




# Long term hydrogen storage properties of ZK60 Mg-alloy as processed by different methods of SPD

P. Cengeri<sup>1</sup>, Y. Kimoto<sup>2</sup>, M. Janoska<sup>3</sup>, Z. Abbasi<sup>1,4</sup>, Y. Morisada<sup>5</sup>, H. Fujii<sup>5</sup>, N. Enzinger<sup>6</sup>, Ch. Sommitsch<sup>6</sup>, G. Boczkai<sup>3</sup>, G. Krexner<sup>1</sup>, M. J. Zehetbauer<sup>1,\*</sup> , and E. Schafner<sup>1</sup>

<sup>1</sup> Faculty of Physics, Univ. Vienna, Wien, Austria

<sup>2</sup> Joining and Welding Research Institute, Osaka University, Osaka, Japan

<sup>3</sup> Faculty of Nonferrous Metals, Univ. Sci & Technology, Krakow, Poland

<sup>4</sup> Institute for Technical Physics, Karlsruhe Institute of Technology, Eggenstein-Leopoldshafen, Germany

<sup>5</sup> Osaka Research Institute of Industrial Science and Technology, Osaka, Japan

<sup>6</sup> Institute of Materials Science, Joining and Forming, TU Graz, Graz, Austria

**Received:** 28 November 2023

**Accepted:** 18 February 2024

**Published online:**  
13 April 2024

© The Author(s), 2024

## ABSTRACT

Hydrogen storage characteristics is studied in the Mg-alloy ZK60 after processing by different SPD (Severe Plastic Deformation) methods such as High Pressure Torsion (HPT) and Friction Stir Processing (FSP), applying various deformation extents and rates. The capacity and kinetics of hydrogen storage was investigated and analysed, up to 100 storage cycles. While the degree of SPD deformation is less important for the storage capacity, the SPD processing method itself matters, yielding about ~ 30% more capacity in FSP than in HPT. As shown by DSC and XRD analyses, it is the density of SPD-induced vacancy agglomerates which is significantly higher in FSP than in HPT ( $\sim 10^{-3}$  instead of  $\sim 10^{-4}$ ) because of the enhanced dislocation slip activity. Thanks to their stabilization through Mg(Zn,Zr) precipitates, the vacancy agglomerates survive numerous cycles of hydrogen storage in spite of the high storage temperature of 350 °C, and can act as thermally stable heterogeneous nuclei for the hydrogenation. This latter mechanism was found in all SPD methods applied irrespective of the deformation extent, on the basis of Johnson–Mehl–Avrami–Kolmogorov analysis providing the Avrami exponent  $n = 1$ , already from the second up to the highest hydrogen storage cycles.

This paper is dedicated to Univ. Prof. Dr.-Ing. habil. Dr. h.c. Jürgen Eckert on the occasion of his 60th birthday.

Handling Editor: Megumi Kawasaki.

Address correspondence to E-mail: michael.zehetbauer@univie.ac.at

## Introduction

With the beginning of the 21st century, methods of renewable energy production and its storage management find increasing interest [1]. Concerning the storage of hydrogen, however, questions remain open (i) whether H can be economically stored in low-mass solid storage systems, and (ii) whether their storage capacity stands even high numbers of storage cycles. Some success has been reported [2–5] by adding various catalyzers and particles to the storage material. Alternatively, recent studies showed that methods of severe plastic deformation (SPD) not only facilitate the storage of hydrogen by making its activation unnecessary [6–8], but also enhances the storage kinetics and storage stability up to high numbers of cycles [9–12]. Apparently, the reasons for this come from the increased densities of SPD induced lattice defects [13]—especially those of vacancies and vacancy agglomerates [10, 12]. In a recent review [14], differences in hydrogen storage performance of Mg alloys deformed by different SPD methods have been discussed, and questions arose whether those differences come from the specific densities or types of the lattice defects of the SPD method considered.

To answer those questions, the present work is devoted to systematic long term hydrogen storage investigations of two different SPD methods, i.e. High Pressure Torsion (HPT) and Friction Stir Processing (FSP), and to comparisons of the effects of these methods. While the long term hydrogen storage kinetics of ZK60 magnesium alloy was already studied for Equal Channel Angular Pressing (ECAP) [10] and HPT [12], for FSP only the work of Silva et al. [15] exists but for not more than 3 absorption/desorption cycles. Moreover, no efforts have been done so far to investigate the influence of deformation degree to the hydrogen storage behaviour. Therefore, like in our previous works on ECAP and HPT processed ZK60 magnesium alloy, the current work was concerned with long term storage of at least 100 cycles of FSP processed samples. As concerns the experiments on HPT processed samples, they have been extended to various deformation degrees. In addition to our previous studies [10, 12], SPD defect analyses by DSC and XRD methods were undertaken to answer the open questions mentioned above.

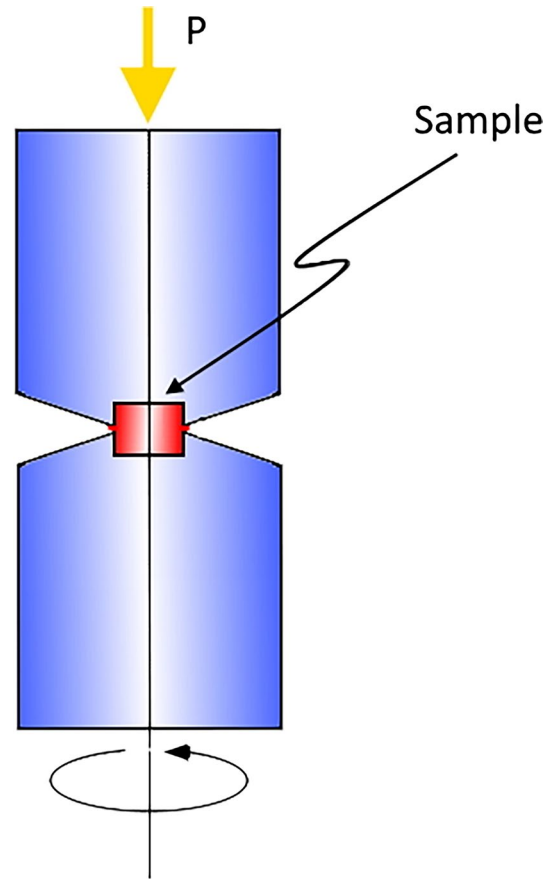


**Figure 1** Schematic depiction of HPT.

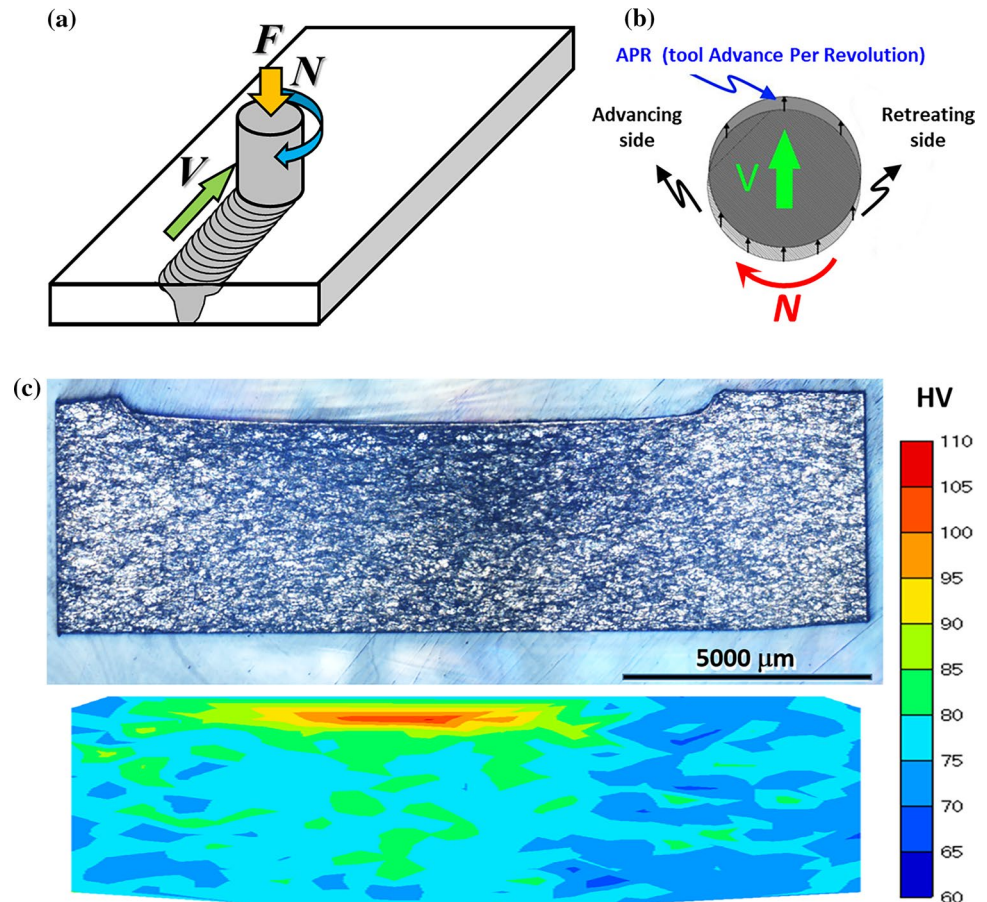
## Experimental: materials and methods

The material used was Mg alloy ZK60, with a nominal composition of 94 wt% Mg, 4.80–6.20 wt% Zn, and  $\geq 0.45$  wt% Zr (according to systems ASTM, SAE). The material used for the HPT samples had a composition of 5.14 wt.% Zn and 0.68 wt.% Zr; it was manufactured and delivered as extruded cylindrical rods with diameter 25.4 mm by METALMART INTERNATIONAL, CA, USA. For FSP processing, extruded plates of Mg alloy ZK60 were used with dimensions  $100 \times 150 \times 4.5$  mm, and a composition of 5.74 wt% Zn and 0.44 wt% Zr, manufactured and delivered by OSAKA FUJI Corporation, Japan.

### HPT (high pressure torsion) processing

A HPT device consists of two anvils with a cavity in the centre, in which the sample is placed. A defined hydrostatic pressure  $P$  is applied, and afterwards,

**Figure 2** **a** Sketch of Friction Stir Processing (FSP), **b** Explanation of quantities being part of Eq. (3), **c**: Optical microscopy image and microhardness map (Vickers) of the stirred zone showing the distribution and intensity of FSP deformation.



deformation starts by rotating one plunger relative to the other (Fig. 1, [16, 17]).

For HPT processing, the rods were cut by spark erosion to discs with radii  $r = 3$  till 5 mm and thicknesses  $d = 0.5$  till 0.8 mm, afterwards cleaned with acetone and finally sand blasted. The discs were deformed at room temperature by rotation numbers  $m = 0.25, 0.5, 1,$  and 2, at a pressure of 4 GPa and a rotation speed of 0.2 rpm. By means of formula (1), the torsional shear strain can be calculated as

$$\gamma = \frac{2\pi m}{d} r \quad (1)$$

This formula only represents the shear strain at the very radius chosen; usually, the maximum radius is taken here. However, across the radius, there is a gradient in strain and accordingly in structure unless the strain is sufficiently large for having reached steady state i.e. saturation. In this case, an effective value  $\gamma_{eff}$ —instead of  $\gamma$  given in (1)—has to be found for optimum characterization of the samples subjected to DSC as well as those to hydrogen

storage measurements. Using the rules of averaging by integration, the effective radius gets  $r_{eff} = r/\sqrt{3}$  and consequently  $\gamma_{eff} = \gamma/\sqrt{3}$ . The equivalent von Mises strain,  $\varepsilon$  (effective von Mises strain  $\varepsilon_{eff}$ ) is obtained by dividing  $\gamma$  ( $\gamma_{eff}$ ) by  $\sqrt{3}$  [16, 17].

### FSP (friction stir processing)

The FSP method is principally based on friction stir welding (FSW) [18–21], Fig. 2. A rotating tool is moving across a plate, and causes a refined microstructure immediately below the tool within the so-called “stir zone”.

According to [21], the local von Mises strain can be calculated as

$$\varepsilon(x) = \ln\left(\frac{l(x)}{APR}\right) + \left| \ln\left(\frac{APR}{l(x)}\right) \right| \quad (2)$$

Here, APR is the tool advance per tool rotation, which is obtained by

$$APR = \frac{v}{dN/dt} \quad (3)$$

with  $v$  being the travel speed, and  $N$  the FSP rotation number (see Fig. 2ab). The elongation  $l(x)$  to which the element of APR is stretched, can be calculated as

$$l(x) = 2D \cos^{-1} \frac{D-x}{D} \quad (4)$$

Here,  $D$  is the pin diameter, and  $x$  is the distance normal to the tool travel direction, from the retreating side of the tool to the streamline in question [20, 21]. The averaged (i.e. effective) von Mises strain for FSP can be estimated as

$$\varepsilon_{eff} = \frac{1}{\sqrt{3}D} \int_0^D \varepsilon(x) dx \quad (5)$$

In this work, two FSP samples were processed at RT, which have been subjected to hydrogen storage experiments. The effective von Mises deformation strains of these samples amount to  $\varepsilon_{eff} = 4.4$  and  $\varepsilon_{eff} = 6.2$ , according to Eqs. (2–5). With both samples, the rotating rate  $dN/dt$  was 100 rpm, with travel speeds  $v = 50$  and 10 mm/min, respectively. In the forthcoming text, these samples are called „FSP Fast “ and „FSP “. The strain rates  $d\varepsilon/dt$  applied were of the order  $\sim 1 \text{ s}^{-1}$ , see [22]. The applied load was 44 kN. The pin-less tool had a cylindrical shape with diameter of 12 mm.

In order to visualize the distribution and intensity of deformation in the FSP stirred zone, not only light micrographs but also microhardness measurements (Vickers) were carried out. The results are part of Fig. 2 showing a cross section of a sample being FSP processed to a von Mises strain  $\varepsilon = 6.2$ . After contact with the rotating FSP tool, there remains a trough at the top of the sample, whose size almost equaled the tool’s diameter of 12 mm. The corresponding microhardness map illustrates clearly that FSP processing of the material does not occur uniformly but gradually decreases with increasing distance from the processed surface.

## Hydrogen storage

The hydrogen storage experiments were performed by means of a specially versatile Sieverts device which has been constructed by M. Krystian [10, 23]. After the SPD treatment in air, samples were transferred into a glove box with an inert Argon atmosphere, thus avoiding

oxidation and/or other contaminations. Within the glove box, the surfaces of the samples were cleaned by sand paper. The sample masses were between 0.053 – 0.076 g in the case of HPT processed samples, and 0.199 – 0.219 g in the case of the FSP processed samples, including those of the as-delivered and filed samples without processing. Still located in the glove box, the samples were entirely filed to chips with sizes between about  $100 \times 100 \text{ }\mu\text{m}$  and  $230 \times 370 \text{ }\mu\text{m}$ , and were deposited in the sample chamber of the Sieverts device. Then the sample chamber was evacuated and heated to 350 °C with the samples still kept under vacuum, allowing for a cleaning of the sample surface for about 30 min. Afterwards, the chamber was loaded with hydrogen reaching pressures of at least 11 bar up to 13 bar, without carrying out any activation process before. After 15 cycles, the chips had a size of 1  $\mu\text{m}$  only (for more details of the microstructure, see Krystian et al. [10]). The desorption was done under subatmospheric pressure of  $< 0.01$  bar. In this work no detailed analyses of the desorption process have been achieved. In order to study the influence of the filing on the storage characteristics, one sample was prepared from the as-delivered material without any SPD processing, that means immediately filed and hydrogenated.

## DSC (differential scanning calorimetry)

The DSC measurements were performed in a heat flux calorimeter type NETZSCH 204. Heating and cooling occurred at a rate of 10 K/min under 99.999% argon atmosphere, from room temperature till 450 °C. All DSC tests have been carried out on as delivered/extruded and filed samples with or without subsequent SPD-processing.

## XRD / XPA (X-ray diffraction / X-ray line profile analysis)

The XRD diffractograms were obtained by BRUKER D-8 DISCOVER X-ray diffractometer equipped with a Bruker VANTEC area detector. The area detector covered up to 35° of  $2\theta$  range at one fixed position, with the  $2\theta$  -position of the detector center at 45°. The  $\omega$ -position of the measured sample was 22.5°. A Cu anode was used for the X-ray radiation operated at 40 kV and 40 mA, with a wavelength of 0.154 nm for  $\text{CuK}\alpha 1$ .

The XPA (X-ray Line Profile Analysis) measurements were performed in a RIGAKU

MM9 rotating anode device operating with monochromatised  $\text{CoK}\alpha$ -radiation at a wavelength of 0.179 nm. The detector in use was an INEL CPS-590 line position quarter circle detector with an angular range between  $40^\circ$  and  $130^\circ$ .

### Analyses of SPD induced defects

Crystallite (coherent domain) sizes and dislocation densities were evaluated by means of the XPA method, using the Modified Williamson-Hall Model introduced by Ungar, see e.g. [24]. The evaluation of XPA data was done by the open source software CMWP-fit (Version 140,518, Budapest, Hungary, [25]).

The concentration of vacancies was determined by combined evaluation of the data gained by XPA and DSC. Evaluation of XPA provided the dislocation density, from which one can calculate the energy ( $E_{disl}$ ) stored in dislocations according to [26] as:

$$E_{disl} = Gb^2 \frac{N}{4\pi\kappa} * \ln \left[ (b\sqrt{N})^{-1} \right] \quad (6)$$

Here,  $G$  is the shear modulus ( $G=17$  GPa),  $b$  the absolute value of the Burgers vector ( $b = 2.26 \times 10^{-10}$  m),  $N$  is the dislocation density, and  $\kappa$  the arithmetic mean of 1 and  $(1-\nu)$ , with  $\nu$  as the Poisson ratio  $\nu=0.35$ , assuming equal parts of edge and screw dislocations.

The energy stored in the vacancies  $E_{vac}$  can be now calculated by subtracting the dislocation energy  $E_{disl}$  from the total energy  $E_{tot}$  obtained from the DSC measurements.

$$E_{tot} - E_{disl} = E_{vac} \quad (7)$$

The vacancy concentration finally follows as:

$$c_v = \frac{E_{vac}}{\Delta H * \chi * N_a} \quad (8)$$

Here,  $\Delta H$  the formation energy of a vacancy ( $= 0.79$  eV [27]),  $\chi$  the mass of sample, and  $N_a$  the Avogadro number.

## Results

### Hydrogen storage behaviour

Figures 3, 4, 5 present the characteristics of the hydrogen storage behaviour for all samples. In agreement with our investigations published in [10] and [12],

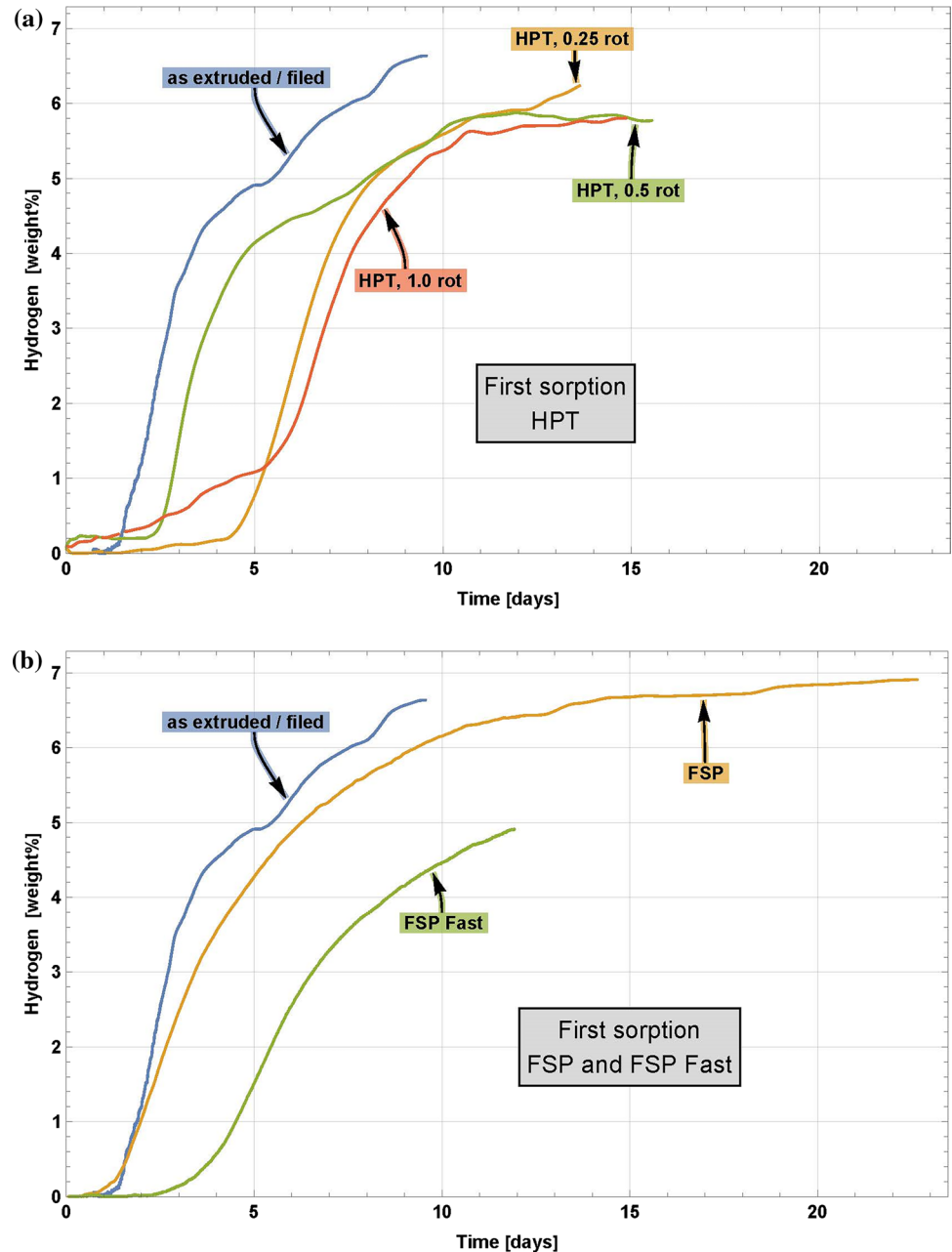
the first storage cycles showed a sigmoidal shape: After starting with an incubation period, a substantial increase of sorption rate occurs which is followed by an asymptotic approach to the thermodynamically possible maximum of hydrogen uptake of the host material given.

Already the second cycles including all following ones—irrespective of the SPD method applied—do not show any incubation period but an immediate strong increase of the hydrogen content. The total hydrogen uptake is the highest during the first loading, again independent of the SPD mode applied. It is important to note here that this result is also true for the sample which has only be filed after delivery and not been SPD deformed at all. This sample's storage characteristics has been added to all Figs. 3–5 for comparison reasons with the SPD processed samples. With all cycles from cycle 1 to cycle 10, the hydrogen uptake clearly decreases, except for the FSP sample named “FSP Fast”, for which no loss was observed. At cycle numbers  $> 10$ , the hydrogen uptake becomes more stable among the SPD processed samples (Figs. 4, 5, and “Role of deformation induced defects for the hydrogen storage capacity”). This is true for all samples processed by HPT by 0.25 to 2 rotations, with respect to both the total hydrogen uptake as well as to the kinetics, even if one inspects the results shown in Fig. 5 and “Role of deformation induced defects for the hydrogen storage capacity” for the highest cycle numbers = 100. Considering the FSP processed samples, the variation of storage capacity as well as the kinetic behaviour is similar: there is a loss in capacity till cycle number 10, but clear stabilization of the capacity occurs for higher uptake numbers till number 100 (Figs. 4b, 5). The highest storage capacity in the hydrogen uptake is shown by the FSP samples which even holds to 100 (Figs. 4b, 5). We conclude that all the SPD processed samples seem to maintain a high stability with on-going cycles; the undeformed samples (i.e. the as-delivered filed ones), however, suffer a stronger loss in the capacity of hydrogen uptake. These stability differences and the possible mechanisms behind are discussed in detail in Sect. “Discussion”.

### DSC and XRD measurements

DSC measurements (Fig. 6) included all samples being processed with different SPD methods, or left undeformed after being delivered and filed. All samples have been investigated without being

**Figure 3** Absolute hydrogen uptake during the 1st loading cycle. **a** HPT processed samples, **b** FSP processed samples. For comparison, the hydrogen uptake of the undeformed (= as extruded / filed) sample is shown, too.



subjected to hydrogenation. All the DSC scans show similar features: At about 70–80 °C (homologous temperature  $T/T_m \sim 0.4$ ,  $T_m$  is the melting temperature in K) and 360–390 °C ( $T/T_m \sim 0.8$ ) there emerge two exotherm peaks whereas at 120–130 °C ( $T/T_m \sim 0.5$ ) and 250–260 °C two endotherm peaks appear. The results of XRD measurements are shown in Fig. 7. In all diffractograms of Fig. 7abc, the peaks of pure Mg appear although with different intensities. Other peaks indicate the occurrence of  $MgZn_2$  especially

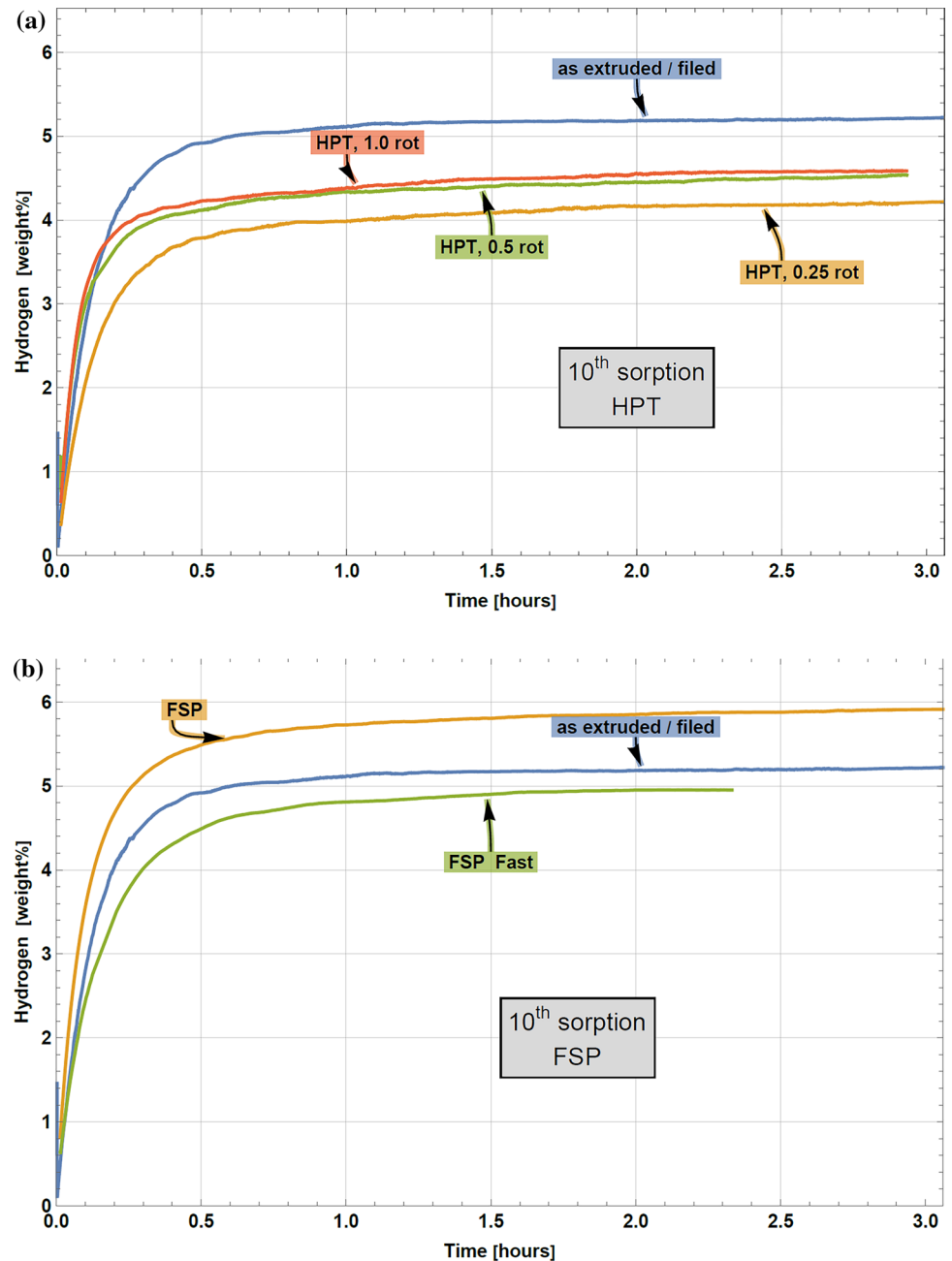
after application of HPT and/or additional thermal treatment between 200–320 °C.

## Discussion

### Role of deformation induced defects for the hydrogen storage capacity

The main aim of this work was to find out which intrinsic material factors are crucial for smart

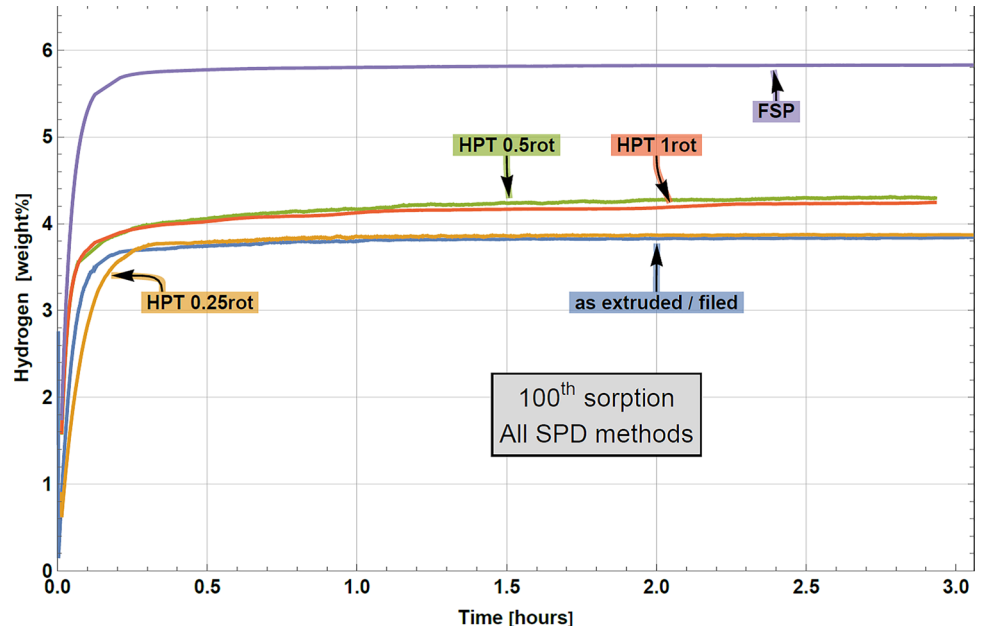
**Figure 4** Absolute hydrogen uptake during the 10th loading cycle. **a** HPT processed samples, **b** FSP processed samples. For comparison, the hydrogen uptake of the undeformed (= as extruded / filed) sample is shown, too.



hydrogen storage with high stability. Already Krystian et al. [10] for ECAP and Grill et al. [12] for HPT processed samples of ZK60 Mg-alloy reported a long term hydrogen storage stability with cycling numbers higher than 10. The current work again comprises HPT processed samples but with much smaller deformations than in [12] and also with DSC analyses of HPT induced lattice defects. Moreover, also results for Friction Stir Processed (FSP) samples are presented. In both cases, long time storage stability

was observed (Figs. 8, & 9). In [12], a model has been suggested which explains this stable high-cycle performance in terms of heterogeneous nucleation of the hydride at thermally stable SPD/deformation induced lattice defects. In this work, importantly, state-of-the-art DSC and X-ray diffraction analyses were undertaken, not only in order to evaluate the nature and density of various SPD induced defects but also to check for the occurrence of any **phase transition** which may play a role for the hydride formation. In

**Figure 5** Absolute hydrogen uptake during the 100th loading cycle, for all the SPD methods HPT and FSP, as well as for the undeformed (= as extruded/ filed) sample.



order to identify stable endo- and exotherm peaks by DSC in an unambiguous way, after the first heating also a second heating was undertaken for all DSC runs where the endotherm peaks reappeared but the exotherm peaks were missing. This confirms our interpretation of the endotherm peaks and exotherm peaks in terms of phase transition and lattice defect annealing, respectively, as explained in detail below.

First of all, we like to understand the two *endotherm peaks 1, 2* appearing in all DSC plots in terms of phase transformations. We are confirmed in this interpretation by the investigations by XRD (Fig. 7): On the one hand, they show that the XRD peaks of the Mg matrix change their intensities individually during SPD processing (Fig. 7, compare (a) and (b)) thus indicating the formation of a shear texture. The peaks which represent the  $\text{MgZn}_2$  phase (exactly speaking, that of  $\text{Mg}(\text{Zn}, \text{Zr})$  phase which shows an only marginally different diffraction angle) appear more pronounced in the SPD processed sample, indicating some SPD induced increased fraction of this phase. On the other hand, the three  $\text{Mg}(\text{Zn}, \text{Zr})$  peaks remain unchanged when the samples get annealed at temperatures 200–320 °C after SPD processing (Fig. 7, compare (b) and (c)). These XRD results are in line with those of the DSC analysis (Fig. 6) where the biggest endotherm peak 2 disappears not before 320 °C meaning that the phase  $\text{Mg}(\text{Zn}, \text{Zr})$  is stable till this temperature. Its

disappearance may be connected with emergence of the biggest *exotherm peak 2* which appears beyond 350 °C in most cases, the latter representing the hydrogen absorption/desorption temperature. The H storage kinetics seems to be rather connected with the exotherm peaks 2 rather than the endotherm peak 2, indicating that the SPD (i.e. HPT or FSP-) induced lattice defects are more important for the kinetics of hydrogen storage than the  $\text{Mg}(\text{Zn}, \text{Zr})$  precipitates, see e.g. Fukai [28]. Nevertheless, the latter may be crucial for the high stability of the SPD induced defects allowing their survival of the H absorption/desorption process (compare Grill et al., [12]).

According to the articles by van den Beukel et al. [29], and Zehetbauer [30], and especially a recent one by Ojdanic et al. [31] on similar Mg alloys, exotherm peaks around  $T \sim 0.3 - 0.45 T_m$  ( $T_m$  is the melting temperature in K)—like peak 1 of this work—can be attributed to single and double vacancies whereas those around  $T \sim 0.55 T_m$  may represent the annealing of dislocations being part of deformation induced subgrain boundaries.

Following the evaluation procedures methods applied in Setman [32], and the recent one by Ojdanic et al. [31], one can check the presence and density of the deformation induced lattice defects such as vacancies, vacancy agglomerates, subgrains and dislocations by a combined evaluation of XPA and DSC (see also



**Figure 6** DSC heating curves of ZK60 samples processed by different SPD methods. **a** HPT with  $\epsilon_{eff}=3.3$  (0.25 rot, green curve),  $\epsilon_{eff}=6.5$  (0.5 rot, blue curve),  $\epsilon_{eff}=13.1$  (1 rot, brown curve), and  $\epsilon_{eff}=45.3$  (2 rot, black curve); **b** FSP ( $\epsilon_{eff}=6.2$ ); **c** extruded/rolled. Exotherm peaks are indicated by black line boxes, endotherm ones by red line boxes.

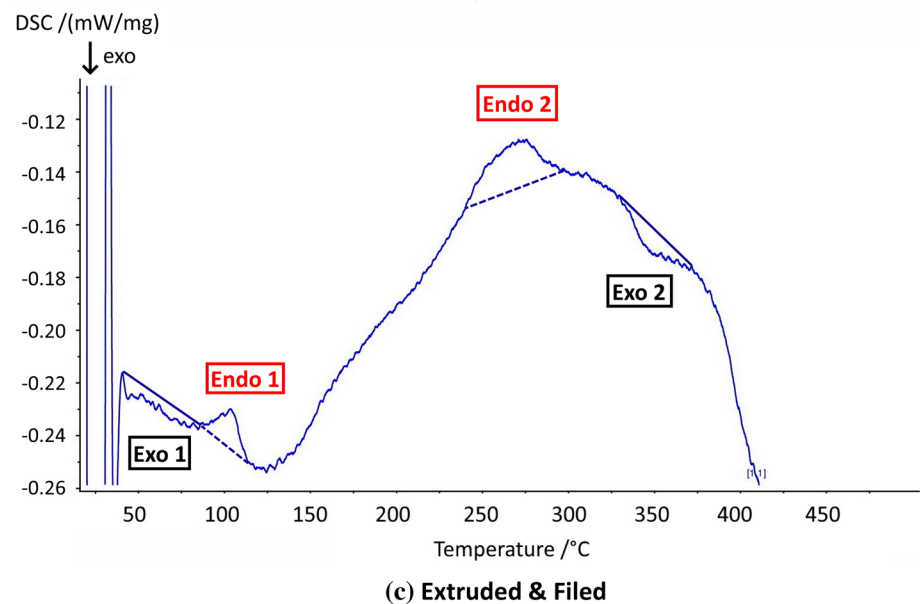
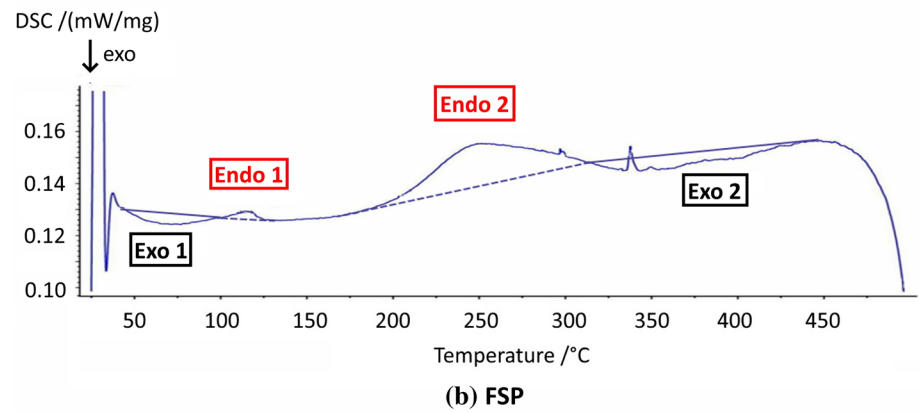
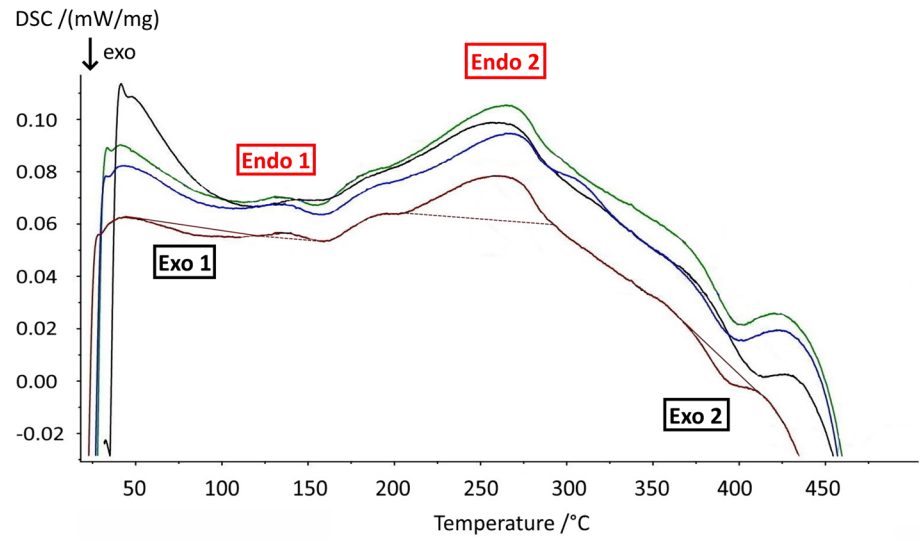


**Figure 7** Peak positions of ZK60 material. **a** Red graph: ZK60 as delivered, **b** blue graph: ZK60 after additional HPT processing by 0.25 rotations, **c** yellow graph: ZK60 after additional HPT processing plus annealing at temperatures between 200 °C up to 320 °C.

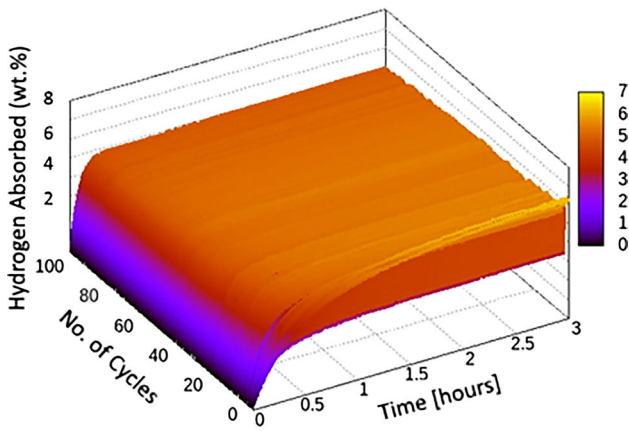
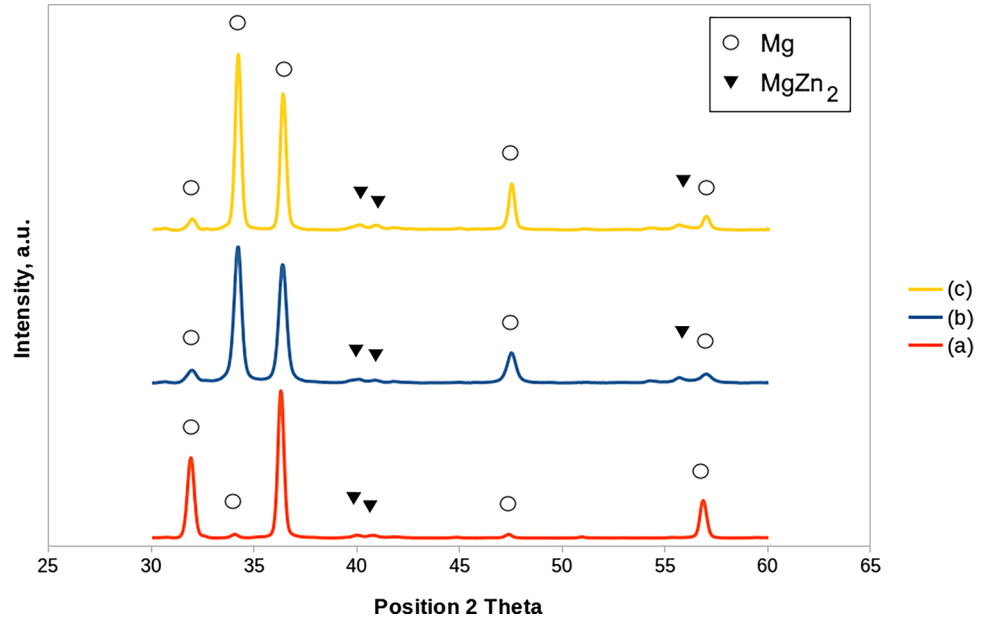


**Figure 8** Hydrogen storage kinetics (sorption) of HPT sample processed by 0.25 rot,  $\epsilon_{eff} \geq 2.2$ .

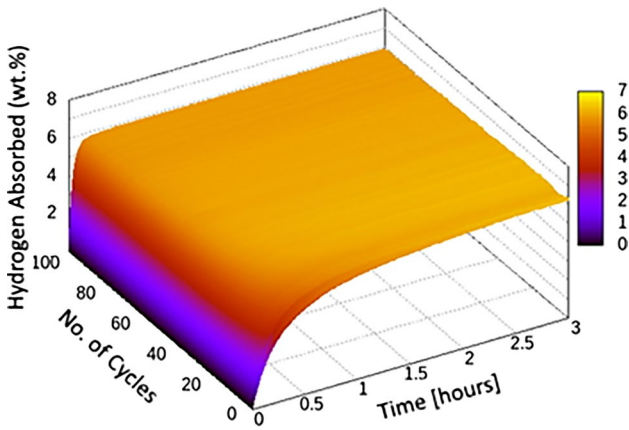


**Figure 9** Hydrogen storage kinetics (sorption) of FSP sample processed to  $\epsilon_{eff} = 6.2$ .

**Table 1** Crystallite sizes for HPT processed samples, as function of annealing temperature and of rotation number. Values are given in units of nm

Crystallite size [nm]	0.25 rot	0.5 rot	1 rot	2 rot
RT	49 ± 4	57 ± 6	46 ± 2	64 ± 4
200 °C	161 ± 5	146 ± 8	157 ± 5	126 ± 5

section experimental details). The procedure was used with the current data, too, and resulted in the values presented in Table 1, 2, 3, 4. It turns out that not only HPT induced vacancies annealed in the exotherm peak but also a significant part of HPT induced dislocations; this decrease is also demonstrated by the increase of crystallite size (Table 3) till a temperature of about 200 °C (0.57  $T_m$ ) meaning that these dislocations were part of crystallite small angle boundaries. Another—equally significant—part of dislocations (the free dislocations left) annealed in the temperature range of the second endotherm peak 2 around 250 °C (0.57  $T_m$ ) with its exotherm heat obviously being far outweighed by the endotherm enthalpy. Summarizing all these findings from XPA, we can conclude that no further annealing of dislocations took place beyond 320 °C (0.72  $T_m$ ) so that the exotherm peak 2 i.e. that around 375 °C (0.79  $T_m$ ) cannot be ascribed to dislocation annealing (Table 1 & 3); rather, it must have been the annealing of the vacancy-type defects with densities of the order  $10^{-4}$ . In view of the high temperature,

**Table 2** Stored energies of the peaks EXO1 and EXO2 representing the specific annealing of SPD induced lattice defects, for various types and extents of SPD processing

Stored Energy [J/g]	rot number	v.Mises equ. strain (eff.) $\epsilon_{eff}$	E(stor) Peak EXO 1 [J/g]	E(stor) Peak EXO 2 [J/g]
HPT	0.25	3.3	−1.66	−2.71
HPT	0.5	6.5	−1.42	−2.30
HPT	1	13.1	−1.22	−0.92
HPT	2	45.3	−1.37	−2.19
FSP	–	6.2	−1.44	−3.59
As deliv. & filed	–	–	−0.97	−2.25

**Table 3** Loss of dislocation density  $\Delta N_{disl}$  for HPT and FSP processed samples in the temperature intervals given, as a function of deformation

$\Delta N_{disl}[10^{15} \text{ m}^{-2}]$	$\Delta N_{RT-200}$ (0.4–0.6 $T_m$ )	$\Delta N_{200-320}$ (0.6–0.7 $T_m$ )	$\Delta N_{320-450}$ (0.7–0.8 $T_m$ )
HPT 0.25 rot/ $\epsilon_{eff}=3.3$	0.09	0.24	0
HPT 0.5 rot/ $\epsilon_{eff}=6.5$	0.18	0.15	0
HPT 1 rot/ $\epsilon_{eff}=13.1$	0.12	0.24	0
HPT 2 rot/ $\epsilon_{eff}=45.3$	0.19	0.10	0
FSP $\epsilon_{eff}=6.2$	0.27	0.27	0

**Table 4** Loss of vacancy concentration ( $\Delta c_{vac}$ ) for HPT and FSP processed samples in temperature intervals given, as a function of deformation

$\Delta c_{vac}$	$\Delta c_{RT-200}$ (0.4–0.6 $T_m$ )	$\Delta c_{200-320}$ (0.6–0.7 $T_m$ )	$\Delta c_{320-450}$ (0.7–0.8 $T_m$ )
HPT 0.25 rot/ $\epsilon_{eff}=3.3$	$1.3 \cdot 10^{-4}$	0	$2.6 \cdot 10^{-4}$
HPT 0.5 rot/ $\epsilon_{eff}=6.5$	$3.3 \cdot 10^{-4}$	0	$6.0 \cdot 10^{-4}$
HPT 1 rot/ $\epsilon_{eff}=13.1$	$2.7 \cdot 10^{-4}$	0	$2.3 \cdot 10^{-4}$
HPT 2 rot/ $\epsilon_{eff}=45.3$	$2.5 \cdot 10^{-4}$	0	$5.8 \cdot 10^{-4}$
FSP $\epsilon_{eff}=6.2$	$5.5 \cdot 10^{-4}$	0	$1.1 \cdot 10^{-3}$

these vacancies have to be thought as vacancy agglomerates which are much more heat resistant compared to single or double vacancies; the same conclusion already resulted from our previous analyses of low-concentration Mg alloys [31].

Again it must be emphasized that the annealing temperature of these defects is 375 °C ( $\sim 0.79 T_m$ ) which is significantly higher than the sorption/desorption temperature of hydrogen storage experiments. It means that these defects withstand the heating ( $\sim 350$  °C i.e.  $0.55 T_m$ ) typical of the hydrogen storage process, so that they can act as thermally stable nuclei

for the hydride formation as suggested by Grill et al. [12]; here, vacancies and/or vacancy agglomerates are predestined to trap hydrogen rather than dislocations the specific free volume of which is smaller [28]. The Mg(Zn,Zr) precipitates may not directly trap the H atoms but work as a stabilizer of the vacancy agglomerates especially when they may be stabilized themselves by a small percentage of Zr in ZK60 alloys [33].

Data of Table 3 also demonstrate that there is no relevant increase of the dislocation density when the deformation degree is increased by HPT from 0.25 to 2 rot (the sum of dislocation densities given in columns 1 & 2 is always about  $0.3 \times 10^{15} \text{ m}^{-2}$ ). The same is true for the value of crystallite size which does not significantly decrease with increasing deformation degree. Both facts suggest that the HPT processing of ZK60 reaches steady state beyond a critical deformation of  $\sim 1$  rot (von Mises strain  $\epsilon \sim 25$ ) which is confirmed by the stress–strain relationships of Mg-5Zn-X alloys reported by Ojdanic et al. [31].

Because the dislocations are the source of vacancy generation [30], it is not surprising that the concentration of single/double vacancies and especially that of vacancy agglomerates saturates with increasing HPT deformation, too (the sum of vacancy concentrations of the two columns of Table 4 equals  $3.9\text{--}8.3 \cdot 10^{-4}$ ) with a slight tendency to higher values with higher strains applied).

Inspecting the saturation hydrogen storage levels after different cycle numbers, they also appear to be largely independent of the HPT deformation degree (Figs. 3, 4, 5, and Table 5). Moreover, they all decrease by up to 20% during the first 10 cycles, probably because of the loss of thermally unstable SPD induced lattice defects: special carefully controlled desorption experiments showed that there have been no residues of hydrogen. For additional cycles beyond 10 till 100, however, the decrease of the saturation hydrogen level was less than about 10% in all cases of HPT and FSP

**Table 5** Evolution of the saturation hydrogen uptake with increasing number of cycles

Saturation Hydrogen Uptake	C1	C2	C10	C100	Rel. loss C1:C2	Rel. loss C2:C10	Rel. loss C10:100
As extruded/filed	6.4	5.9	5.5	3.8	0.06	0.07	0.29
HPT 0.25 rot $\epsilon_{eff}=2.2$	> 5.9	5.2	> 4.4	3.9	> 0.12	< 0.15	> 0.11
HPT 0.5 rot $\epsilon_{eff}=5.3$	5.4	4.9	4.5	4.3	0.09	0.08	0.04
HPT 1.0 rot $\epsilon_{eff}=12.6$	5.5	4.9	4.6	4.3	0.11	0.06	0.07
FSP fast $\epsilon_{eff}=4.4$	>> 4.9	5.6	5.0	-	<< 0.14	0.11	-
FSP $\epsilon_{eff}=6.2$	6.9	6.3	6.1	5.9	0.09	0.03	0.03

Values with a (<) or (>) mean that the saturation value could not be reached within the usual sorption time thus affecting the value of relative loss. The values of  $\epsilon_{eff}$  denote the effective von Mises equivalent strains applied with the SPD method given. Those of HPT samples used for hydrogen uptakes little differ from those used for the DSC measurements because of inevitable variations in sample diameter and thickness

processed samples, except those which have not been deformed at all: here, the decrease amounted to more than 20% indicating that the density of thermally stable defects also significantly decreased.

Considering now the saturation hydrogen storage levels of the FSP processed samples after different cycle numbers (Figs. 3, 4, 5, and Table 5), it turns out that these are about 30% higher than those of the HPT processed samples, irrespective of the cycle number considered. After about 10% decrease till cycle 10, there is no decrease at all observed for the higher cycle numbers. Inspecting the corresponding densities of the vacancy agglomerates, these are about the order of  $10^{-3}$  which is a factor 2–5 higher in FSP than those produced in the HPT processed samples. The reason may be the activation of a maximum of slip systems because of the multidirectional character of deformation, which is true already for cyclic deformation [30, 34], and which may play a role especially in anisotropic hcp materials. The enhanced density of vacancy agglomerates may also explain the comparably large hydrogen storage saturation of 5.5. Whatever may be the reason for the high vacancy agglomerate density, we can conclude and understand that its extent is essential for the saturation hydrogen storage level; the fact that this level is definitely stable beyond cycle 10 confirms this conclusion, again in line with the stability of these vacancy agglomerates at the used hydrogen storage temperature of  $T = 350$  °C.

As the as-delivered/hot extruded samples have been routinely filed before the SPD processing [9,10, 12], it was interesting to learn whether and to what extent this filing had an influence on the kinetics and/or hydrogen storage potential of the samples. For this purpose as-delivered/hot extruded samples

were filed before applying any further SPD processing and hydrogen storage procedure. The results were surprising: As shown in all Figs. 3, 4, 5, and Table 5, the absorbed hydrogen percentage of filed samples was almost equal to those of all HPT processed samples, and also the loss in storage capacity till cycle 10 was similar to the SPD processed samples. However, between cycles 10 and 100, a strong decrease of storage capacity occurred which did not happen with the additionally SPD processed samples. Inspection of DSC data for a closer defect trapping analysis showed that all peaks including the relevant one EXO 2 exhibit similar defect densities than those of the SPD methods applied. Thus, for a first explanation, the defect densities are high enough to account for the surprisingly high hydrogen storage saturation level but not the deterioration of storage capacity in long cycle behaviour. It could be that the relative fraction of dislocation numbers compared to the number of vacancy type defects is markedly higher than these fractions are with the SPD methods, thus indicating the loss of favoured trapping sites for the hydrogen to be stored.

### Analysis of storage mechanisms in terms of the JMAK theory

Following our publication by Grill et al. [12], a Johnson–Mehl–Avrami–Kolmogorov (JMAK) analysis [35–40] was carried out with the current data in order to shed more light on the mechanisms of hydrogen storage kinetics, now applied also to HPT processed ZK60 samples with lower deformation degrees than reported in [12], and to a further deformation method being completely different from ECAP and HPT, i.e. Friction Stir Processing (FSP). Again, special attention

has been given to the high cycling stability. Recent studies of our group report that the potential of hydrogen storage of ECAP processing appears to be higher than that of HPT but still remains significantly below that of FSP [14, 41].

The JMAK analysis can quantitatively describe the formation of a new phase which in our case is the hydride phase. The time dependence of the volume fraction of the new phase follows the equation

$$f(t) = 1 - e^{-Ct^n} \quad (9)$$

where  $C$  is a constant related to the geometry of the nuclei of the hydride, and  $n$  the so-called Avrami exponent taking on certain values representing specific mechanisms for nucleation and growth i.e.  $n > 1$  for homogeneous, and  $n = 1$  for heterogeneous growth [12, 35, 38–40, 42]. From Eq. (9) one can derive  $\ln[-\ln(1 - f(t))] = \ln C + n \star \ln t$ , allowing for evaluation of  $n$  as the slope of the graphs (“Avrami plots”) given in Fig. 10 and Table 6.

For all processing methods and irrespective of the extent of deformation, the outcome is similar: In the first cycle,  $n$  equals 2, 3 or even larger values in early hydrogen storage, and finally reaches  $n \sim 1$ . Already in the second cycle, however, only one value is left amounting to  $n = 0.8 \dots 1$ . From cycles 10 and higher, this value approaches  $n \sim 1$  and remains constant with the highest cycles studied. Using the scheme of Avrami exponent analysis reviewed by Torrens-Serra et al. [42], the current hydriding mechanism corresponds to a constant number of nuclei (the Mg(Zn,Zr) particles and vacancy agglomerates) connected with diffusional two-dimensional growth. The latter conclusion is in agreement with previous JMAK analyses although they have been carried out in pure Mg [43, 44].

According to our findings in [12], the reported  $n$  values suggest that with the first cycle, the nucleation of hydride occurs fairly homogeneously ( $n > 1$ ) at the beginning of the hydrogen storage process, and turns to heterogeneity at later storage times. Already at cycle 2, however, only heterogeneous nucleation of the hydride takes place ( $n = 1$ ) during the entire storage process, which holds also for the higher cycle numbers up to 100. These results have to be considered in the context of the nature and density of HPT induced lattice defects being present after different deformation methods and extents. It follows that homogeneous nucleation during the first hydrogen cycle occurs when the small defects like single/double vacancies

and dislocations are present unless they have been already annealed. Such annealing apparently occurs during all storage cycles where only the thermally stable defects i.e. vacancy agglomerates survive: those appear to be solely responsible for the heterogeneous nucleation of the hydride phase [10, 12, 28].

Let us analyse – now also in terms of the JMAK model – the storage characteristics of samples which were not deformed at all. Again, the results for the Avrami exponents for the only filed samples are very similar to that for the deformed samples: Heterogeneous nucleation occurs at the same storage times and cycle numbers. The only difference to the SPD processed sample remains the deterioration of the hydrogen storage capacity for cycle numbers higher than 10. Careful inspection of Table 5 shows that some marked loss of storage capacity also occurs with the smallest HPT deformed sample ( $m = 0.25$  rot). Again, the relative loss of vacancy type defects related to the total defect density may be the reason, being a special feature of samples with comparably small deformation like filed and/or slightly torsioned samples (which both have largely shear deformation character). Further investigations for quantitative determination of the densities of specific defects may shed more light on this question. Concerning filed samples, Asselli et al. [45] already investigated the H storage kinetics and capacity of Mg chips with different geometries, and found their excellent performance in comparison to ball milled materials, not at least because of suppressed oxidation. However, their investigation was limited to two storage cycles only which may explain some differences to the results obtained in the present work.

## Summary and conclusions

In this work, different SPD processing methods (namely HPT and FSP) have been applied to samples of Mg alloy ZK60, and their hydrogen storage characteristics have been studied in detail, with emphasis on high cycle numbers up to 100 (called “final storage” below). The results were as follows:

- (1) The SPD method chosen is clearly affecting the final hydrogen storage capacity of the storage material. The reason seems to be the density of SPD induced defects, especially those of vacancy type, which –

**Figure 10** **a** Avrami plot of the sorption characteristics of HPT sample deformed by 0.25 rot ( $\epsilon_{eff}=2.2$ ) exhibiting  $n > 1$  for the first sorption, and  $n \sim 1$  for all higher sorptions. **b** Avrami plot of the sorption characteristics of two FSP samples deformed by  $\epsilon_{eff}=4.5$  and  $\epsilon_{eff}=6.2$  exhibiting  $n > 1$  for the first sorption, and  $n \sim 1$  for all higher sorptions. **c** Avrami plot of the sorption characteristics of the as extruded/ filed (undeformed) sample exhibiting  $n > 1$  for the first sorption, and  $n \sim 1$  for all higher sorptions.

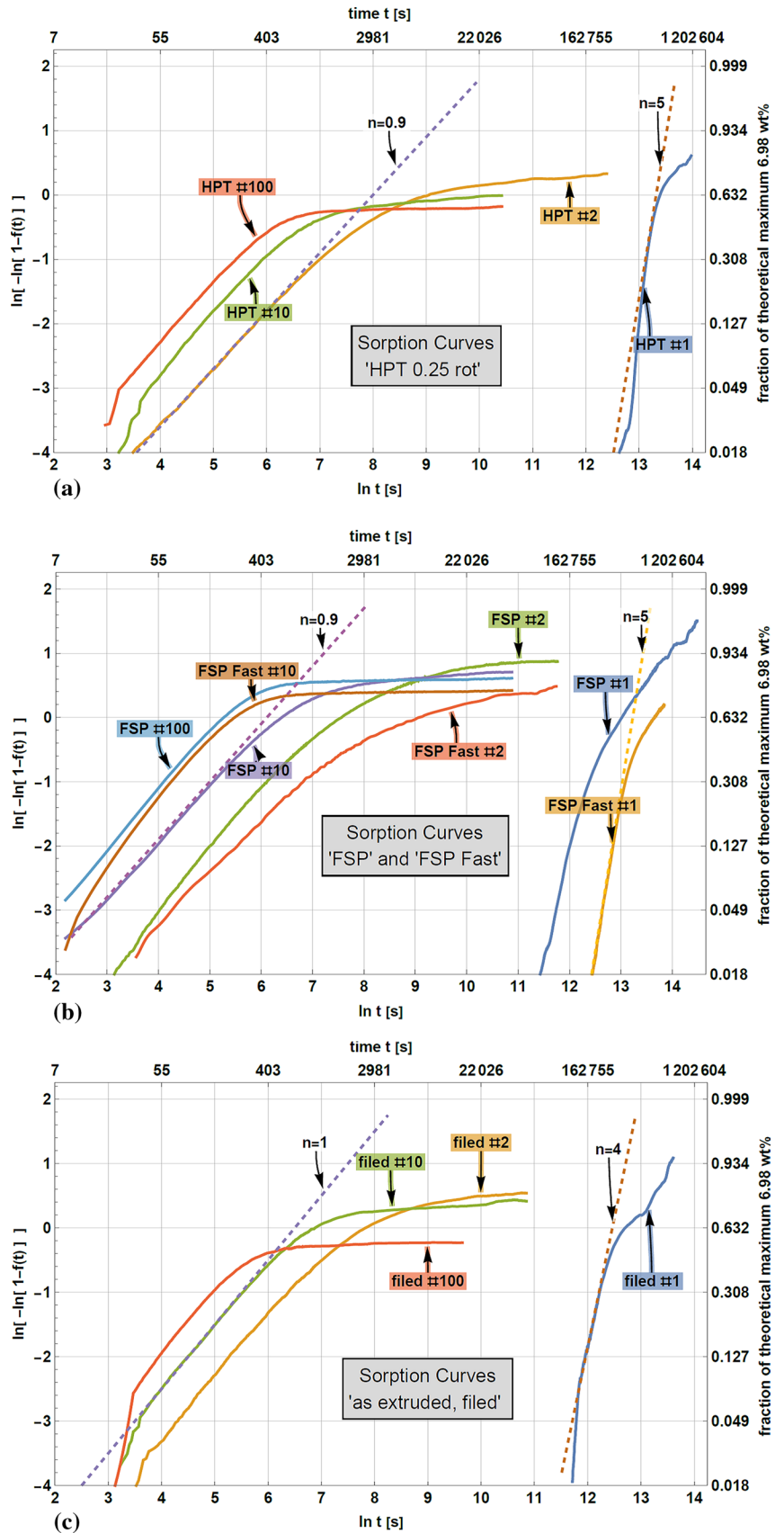


**Table 6** Avrami exponents  $n$ , for all ZK60 samples presented in Table 5. The error amounts to  $dn = \pm 0.1$  because of variations of pressure and of sample masses

Avrami Exponent, $n$	Cycle 1	Cycle 2	Cycle 10	Cycle 100
As extruded/ filed	12.0...4.0...1.0	1.0	1.0	$1.0 \pm 0.1$
HPT 0.25 rot $\varepsilon_{eff} = 2.2$	12.0...7.0...1.0 4.5 (averg)	0.9–1.0	1.0	1.0
HPT 0.5 rot $\varepsilon_{eff} = 5.3$	12.0...2.0...1.0	0.8	1.0	1.0
HPT 1.0 rot $\varepsilon_{eff} = 12.6$	6.0...2.5...1.5	0.9	1.0	1.0
HPT2.0 rot $\varepsilon_{eff} = 36.3$ (Grill, [12])	–	–	1.0	1.2
FSP fast $\varepsilon_{eff} = 4.4$	5.0...1.2 5.0 (averg)	0.8	0.9	–
FSP $\varepsilon_{eff} = 6.2$	4	0.9	0.9	1.0

while comparing deformations of different SPD methods with the same effective equivalent strain—apparently depends on the number of active slip systems of the SPD method chosen.

- (2) For one and the same SPD method, however, the deformation strain applied does not play a role for the storage capacity at least when a critical strain achieving steady state deformation conditions has been reached. At smaller strains, the final storage capacity seems to be smaller probably because of the smaller density of SPD induced defects produced. The tests with smaller deformation not only comprised HPT samples but also those which were only filed after extrusion.
- (3) Extensive JMAK analyses in combination with XRD and DSC studies showed that the mechanism responsible for the hydrogen storage is the trapping of hydrogen at SPD induced vacancy agglomerates which nucleate at Mg(Zn,Zr) precipitates being present in the ZK60 Mg alloy till temperatures beyond the hydrogen storage temperature.
- (4) For all storage processes, the Avrami exponent turned out to be  $n \sim 1$  already from the second cycle till the highest i.e. 100 cycles studied, irrespective of SPD method or deformation strain applied.  $n = 1$  indicates the case of constant density of nuclei and diffusion controlled 2-dimensional growth.

## Acknowledgements

This research was supported by the Austrian Research Promotion Agency (FFG) within project 838668 H2DE-SORB within the call e!MISSION.at. Further funding was given by dedicated research grants of the Toyota Mobility Foundation (TMF), Japan, and of the AMADA Foundation, Japan.

## Author contributions

Not applicable.

## Funding

Open access funding provided by University of Vienna.

## Data and code availability

All publications in the list of references are assigned a DOI number and are available in case of open access. Ref. [25] contains a web address with free access to a programme allowing for determination of dislocation densities and coherently scattering domain sizes.

## Declarations

**Conflicts of interest** The authors declare that there are neither relationships nor interests of them that could potentially influence or bias the submitted work.

**Ethical approval** Not applicable.

**Open Access** This article is licensed under a Creative Commons Attribution 4.0 International License, which permits use, sharing, adaptation, distribution and reproduction in any medium or format, as long as you give appropriate credit to the original author(s) and the source, provide a link to the Creative Commons licence, and indicate if changes were made. The images or other third party material in this article are included in the article's Creative Commons licence, unless indicated otherwise in a

credit line to the material. If material is not included in the article's Creative Commons licence and your intended use is not permitted by statutory regulation or exceeds the permitted use, you will need to obtain permission directly from the copyright holder. To view a copy of this licence, visit <http://creativecommons.org/licenses/by/4.0/>.

## References

- [1] Dornheim M, Eigen N, Barkhordarian G, Klassen T, Bormann R (2006) Tailoring hydrogen storage materials towards application. *Adv Eng Mater* 8:377–385. <https://doi.org/10.1002/adem.200600018>
- [2] Dehouche Z, Djaozandry R, Huot J, Boily S, Goyette J, Bose TK et al (2000) Influence of cycling on the thermodynamic and structure properties of nanocrystalline magnesium based hydride. *J Alloys Comp* 305:264–271. [https://doi.org/10.1016/S01025-8388\(00\)00718-0](https://doi.org/10.1016/S01025-8388(00)00718-0)
- [3] Wu Ch, Wang P, Yao X, Liu C, Chen D, Lu GQ, Cheng H (2005) Effects of SWNT and metallic catalyst on hydrogen absorption/desorption performance of MgH<sub>2</sub>. *J Phys Chem B* 109(47):22217–22221. <https://doi.org/10.1021/jp0545041>
- [4] Fu Y, Kulenovic R, Mertz R (2008) The cycle stability of Mg-based nanostructured materials. *J Alloys Comp* 464:374–376. <https://doi.org/10.1016/j.jallcom.2007.010.1210>
- [5] Huang SJ, Lai CJ, Rajagopal V, Chang WL (2023) Enhancing hydrogen storage in AZ31 alloy through Pd/G composite. *J Res Updates Polymer Sci* 12:203–207. <https://doi.org/10.6000/1929-5995.2023.12.18>
- [6] Edalati K, Matsuda J, Iwaoka H, Toh S, Akiba E, Horita Z (2012) High-pressure torsion of TiFe intermetallics for activation of hydrogen storage at room temperature with heterogeneous nanostructure. *Int J Hydrogen Energy* 38:4622–4627. <https://doi.org/10.1016/j.ijhydene.2013.01.185>
- [7] Edalati K, Matsuda J, Yanagida A, Akiba E, Horita Z (2014) Activation of TiFe for hydrogen storage by plastic deformation using groove rolling and high-pressure torsion: similarities and differences. *Int J of Hydrogen Energy* 310:155810–215594. <https://doi.org/10.1016/j.ijhydene.2014.07.124>
- [8] Edalati K, Matsuda J, Arita M, Daio T, Akiba E, Horita Z (2013) Mechanism of activation of TiFe intermetallics for hydrogen storage by severe plastic deformation using high-pressure torsion. *Appl Phys Lett* 103:3902. <https://doi.org/10.1063/1.4823555>
- [9] Skripnyuk VM, Rabkin E, Estrin Y, Lapovok R (2004) The effect of ball milling and equal channel angular pressing on the hydrogen absorption/desorption properties of Mg-4.95 wt% Zn-0.71wt% Zr(ZK60) alloy. *Acta Mater* 52:405–414. <https://doi.org/10.1016/j.actamat.2003.09.025>
- [10] Krystian M, Zehetbauer MJ, Kropik H, Mingler B, Krexner G (2011) Hydrogen storage properties of bulk nanostructured ZK60 Mg alloy processed by equal channel angular pressing. *J Alloys Comp* 509S:S449–S455. <https://doi.org/10.1016/j.jallcom.2011.01.029>
- [11] Huot J, Skryabina NY, Fruchard D (2012) Application of severe plastic deformation techniques to magnesium for enhanced hydrogen sorption properties. *Metals* 2:329–343. <https://doi.org/10.3390/met2030329>
- [12] Grill A, Horky J, Panigrahi A, Krexner G, Zehetbauer M (2015) Long-term hydrogen storage in Mg and ZK60 after severe plastic deformation. *Int J of Hydrogen Energy* 40:17144–17152. <https://doi.org/10.1016/j.ijhydene.2015.05.145>
- [13] Huang SJ, Rajagopal V, Skripnyuk V, Rabkin E, Fang Ch (2023) A comparative study of hydrogen storage properties of AZ31 and AZ91 magnesium alloys processed by different methods. *J Alloys Comp* 935–1:167854. <https://doi.org/10.1016/j.jallcom.2022.167854>
- [14] Edalati K, Akiba E, Botta WJ, Estrin Y, Floriano R, Fruchard D, Grosdidier T, Horita Z, Huot J, Li HW, Lin HJ, Révész A, Zehetbauer MJ (2023) ch. 3.3. in *Impact of severe plastic deformation on kinetics and thermodynamics of hydrogen storage in magnesium and its alloys*. *J Mater Sci Techn* 146:221–239. <https://doi.org/10.48550/arXiv.2301.05009>
- [15] Silva EP, Leiva DR, Pinto HC, Floriano R, Neves AM, Botta WJ (2018) Effects of friction stir processing on hydrogen storage of ZK60 alloy. *Int J of Hydrogen Energy* 43:11085–11091. <https://doi.org/10.1016/j.ijhydene.2018.04.209>
- [16] Zhilyaev T, Langdon A (2008) Using high-pressure torsion for metal processing: fundamentals and applications. *Prog Mater Sci* 53:893–979. <https://doi.org/10.1016/j.pmatsci.2008.03.002>
- [17] Pippin R (2009) High-pressure torsion—features and applications, ch. 9 in: *Bulk nanostructured materials*, eds. Zehetbauer MJ, Th Zhu Y, Wiley VCH <https://doi.org/10.1002/9783527626892.ch9>
- [18] Thomas WM, Nicholas ED, Needham JC, Murch MG, Temple-Smith P, Dawes CJ (1991). International patent application No. PCT/GB92/02203 and GB patent application No.9125978.8.
- [19] Mishra RS, Ma ZY (2005) Friction stir welding and processing. *Mater Sci Eng A* 50:1–78. <https://doi.org/10.1016/j.mser.2005.07.001>
- [20] Ma ZY, Feng AH, Chen DL, Shen J (2017) Recent advances in friction stir welding/processing of aluminium alloys: microstructural evolution and mechanical properties. *Crit Rev Solid State Mater Sci* 43:1–65



- [21] Reynolds AP (2007) Flow visualization and simulation in FSW. *Scri Mater* 58:338–342. <https://doi.org/10.1016/j.scriptamat.2007.10.048>
- [22] Chang CI, Lee CJ, Huang JC (2004) Relationship between grain size and Zener-Hollomon parameter during friction stir processing in AZ31 Mg alloys. *Scripta Mater* 51:509–514. <https://doi.org/10.1016/j.scriptamat.2004.05.043>
- [23] Kropik H (2008) Wasserstoffspeicherung in SPD-nanokristallisierten ZK60 Magnesiumlegierungen, Master Thesis (in German). University of Vienna, Wien, Austria
- [24] Ungár T, Borbély A (1995) The effect of dislocation contrast on X-ray line broadening: a new approach to line profile analysis. *Appl Phys Lett* 69:3173–3175. <https://doi.org/10.1063/1.117951>
- [25] Convolutional multiple whole profile fitting main page. Available online: <http://csendes.elte.hu/cmwp/> (accessed on 27 March 2020).
- [26] Bever MB, Holt DL, Titchener AL (1973) The stored energy of cold work. *Prog Mater Sci* 17:5–177. [https://doi.org/10.1016/0079-6425\(73\)90001-7](https://doi.org/10.1016/0079-6425(73)90001-7)
- [27] Tzanetakis P, Hillairet J, Revel G (1976) The formation energy of vacancies in aluminium and magnesium. *Phys Stat Sol (b)* 75:433–439. <https://doi.org/10.1002/pssb.2220750205>
- [28] Fukai H (2003) Formation of superabundant vacancies in M<sub>2</sub>H alloys and some of its consequences: a review. *J Alloys Comp* 356–357:263–269. [https://doi.org/10.1016/S0925-8388\(02\)01269-0](https://doi.org/10.1016/S0925-8388(02)01269-0)
- [29] Van den Beukel A (1969), in: *Vacancies and interstitials in metals*, eds. Seeger A et al., North Holland, Amsterdam, p.427–479
- [30] Zehetbauer MJ (1994) Effects of non-equilibrium vacancies on strengthening. *Key Eng Mater* 97–98:287–306. <https://doi.org/10.4028/www.scientific.net/KEM.97-98.287>
- [31] Ojdanic A, Horky J, Mingler B, Fanetti M, Gardonio S, Valant M, Sulkowski B, Schafner E, Dmytro O, Zehetbauer MJ (2020) The effects of severe plastic deformation and/or thermal treatment on the mechanical properties of bio-degradable Mg-Alloys. *Metals* 10:1064. <https://doi.org/10.3390/met10081064>
- [32] Setman D, Schafner E, Korznikova E, Zehetbauer MJ (2008) The presence and nature of vacancy type defects in nanometals detained by severe plastic deformation. *Mater Sci Eng A* 493:116–122. <https://doi.org/10.1016/J.MSEA.2007.06.093>
- [33] Bhattacharjee T, Mendis CL, Sasaki TT, Ohkubo T, Hono K (2012) Effect of Zr addition on the precipitation in Mg-Zn-based alloy. *Scripta Mater* 67:967–970. <https://doi.org/10.1016/j.scriptamat.2012.08.031>
- [34] Polak J (2020) Production, annihilation and migration of point defects in cyclic straining. *Materialia* 14:100938. <https://doi.org/10.1016/j.mtla.2020.100938>
- [35] Christian JW (2002) *The theory of transformations in metals and alloys part I*. Pergamon Press
- [36] Kolmogorov NN (1937) On the statistical theory of the crystallization of metals. *Bull Acad Sci USSR* 1:355
- [37] Johnson WA, Mehl RF (1939) Reaction kinetics in processes of nucleation and growth. *Trans Metall Soc AIME* 135:416–442
- [38] Avrami M (1939) Kinetics of phase change I. general theory. *J Chem Phys* 7:1103–1112. <https://doi.org/10.1063/1.1750380>
- [39] Avrami M (1940) Kinetics of phase change II. transformation-time relations for random distribution of nuclei. *J Chem Phys* 8:212–224. <https://doi.org/10.1063/1.1750631>
- [40] Avrami M (1941) Kinetics of phase change III. granulation, phase change, and microstructure kinetics of phase change. *J Chem Phys* 9:177–184. <https://doi.org/10.1063/1.1750872>
- [41] Abbasi Z, Cengeri P, Krexner J, Zehetbauer MJ, Schafner E (2024) Hydrogen storage properties of Mg-Zn-Gd-Y-Nd alloy processed by SPD, Materials, to be submitted
- [42] Torrens-Serra J, Venkataraman Sh, Stoica M, Kuehn U, Roth S, Eckert J (2011) Non-isothermal kinetic analysis of the crystallization of metallic glasses using the master curve method. *Materials* 4:2231–2243. <https://doi.org/10.3390/ma4122231>
- [43] Mooij L, Dam B (2013) Nucleation and growth mechanisms of nano Mg hydride from the hydrogen sorption kinetics. *Phys Chem Chem Phys* 15:11501. <https://doi.org/10.1039/C3CP51735G>
- [44] Takeichi N, Sakaida Y, Kiyobayashi T, Takeshita HT (2014) Hydrogen absorption and desorption behavior of magnesium hydride: incubation period and reaction mechanism mater. *Trans* 55:1161–1167. <https://doi.org/10.2320/matertrans.MG201405>
- [45] Asselli AAC, Santos SF, Huot J (2016) Hydrogen storage in filed magnesium. *J Alloys Comp* 687:586–594. <https://doi.org/10.1016/j.jallcom.2016.06.109>

**Publisher's Note** Springer Nature remains neutral with regard to jurisdictional claims in published maps and institutional affiliations.